

# Mechanism of Bi–Ni Phase Formation in a Microwave-Assisted Polyol Process

Matthias Smuda,<sup>[a]</sup> Christine Damm,<sup>[b]</sup> Michael Ruck,<sup>[a, c]</sup> and Thomas Doert<sup>\*[a]</sup>

Typically, intermetallic phases are obtained in solid-state reactions or crystallization from melts, which are highly energy and time consuming. The polyol process takes advantage of low temperatures and short reaction times using easily obtainable starting materials. The formation mechanism of these intermetallic particles has received little attention so far, even though a deeper understanding should allow for better synthesis planning. In this study, we therefore investigated the formation of BiNi particles in ethylene glycol in a microwave-assisted polyol process mechanistically. The coordination behavior in solution was analyzed using HPLC-MS and UV-Vis.

Tracking the reaction with PXRD measurements, FT-IR spectroscopy and HR-TEM revealed a successive reduction of Bi<sup>3+</sup> and Ni<sup>2+</sup>, leading to novel spherical core-shell structure in a first reaction step. Bismuth particles are encased in a matrix of nickel nanoparticles of 2 nm to 6 nm in diameter and oxidation products of ethylene glycol. Step-wise diffusion of nickel into the bismuth particle intermediately results in the bismuth-rich compound Bi<sub>3</sub>Ni, which consecutively transforms into the BiNi phase as the reaction progresses. The impacts of the anion type, temperature and pH value were also investigated.

## 1. Introduction

Over the last two decades, nanoparticles composed of two or more metal elements have achieved a great scientific and technological interest due to their special optical and electronic properties. These intermetallic particles often display superior properties in catalysis and electronics.<sup>[1–3]</sup> Various methods to synthesize intermetallic nanomaterials have been developed so far, each with its own benefits and drawbacks. The most common preparation techniques are the co-reduction and thermal annealing.<sup>[4]</sup> Further preparation methods, like thermal decomposition, arc discharge and reverse micelle method are also used in special cases.<sup>[5]</sup> Most of these synthesis methods have disadvantages in either control of morphology, yield, or conformity to green chemistry.<sup>[6,7]</sup>

A very useful and facile method to obtain monometallic or intermetallic particles is the polyol process.<sup>[8]</sup> It uses a broad spectrum of polyalcohols (polyols), which generally have a

threefold purpose in the synthesis, as they serve as solvents, capping agents, and reduction agents. Metal salt precursors have a similar dissolution behavior in polyols as in water due to the chelating effect of the solvent.<sup>[9]</sup> This chelating effect is also advantageous in controlling the particle growth and morphology and it prevents agglomeration of the prepared particles.<sup>[10]</sup> Additionally, the polyol is easily disposed-off due to its non-toxic and non-volatile nature. Last, the polyol is used to reduce the metal to its zero-valent state. The reduction power of a given polyol increases with rising temperature. Therefore, higher temperatures are necessary to obtain particles of metals with lower redox potentials.<sup>[11]</sup> Higher temperatures usually also lead to a higher crystallinity of the particles. In general, the reaction temperatures are limited by the boiling points of the polyols. Higher polyols have higher boiling temperatures, but lower reduction potentials.<sup>[11]</sup> The low energy and time requirements to obtain intermetallic phases in a facile way make the polyol process attractive for industrial application.<sup>[12]</sup>


In comparison to solvothermal syntheses in steel autoclaves, the reaction progress in microwave-assisted synthesis, using glass vessels, can be controlled in situ, and reaction parameters can be adjusted accordingly. Additionally, the closed system provides access to temperatures above the boiling point, granting increased reduction power of the polyol. Reactions can be performed within minutes, due to very fast heating rates and rather homogeneous heat distribution inside the vessel provided by stirring.


With this setup, several intermetallic compounds have been synthesized in quantitative yields. Heise et al. synthesized a plethora of intermetallic nanoparticles using various element combinations.<sup>[13–15]</sup> Even though the polyol process itself was studied and developed intensively over the last 30 years, there are still many details uncovered. Especially for intermetallic particles, little is known about the reaction and formation mechanism. Schaak et al. performed a number of syntheses of

[a] M. Smuda, Prof. Dr. M. Ruck, Prof. Dr. T. Doert  
Faculty of Chemistry and Food Chemistry  
Technische Universität Dresden  
01062 Dresden (Germany)  
E-mail: thomas.doert@tu-dresden.de

[b] C. Damm  
Leibniz Institute for Solid State and Materials Research  
Helmholtzstr. 20  
01069 Dresden (Germany)

[c] Prof. Dr. M. Ruck  
Max Planck Institute for Chemical Physics of Solids  
Nöthnitzer Str 40  
01187 Dresden (Germany)

 Supporting information for this article is available on the WWW under <https://doi.org/10.1002/open.202000236>

 © 2020 The Authors. Published by Wiley-VCH GmbH. This is an open access article under the terms of the Creative Commons Attribution Non-Commercial NoDerivs License, which permits use and distribution in any medium, provided the original work is properly cited, the use is non-commercial and no modifications or adaptations are made.

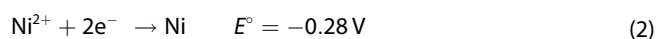
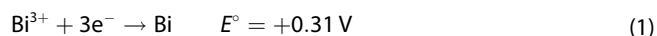
binary and ternary intermetallic compounds.<sup>[16–18]</sup> They systematically studied the formation of selected particles to elucidate the reaction mechanism and the influence of the solvents.<sup>[18,19]</sup>

In the present study, the formation of bismuth-nickel particles, especially due to the interesting superconducting ferromagnetic behavior of micro- and nanostructured Bi<sub>3</sub>Ni<sup>[18,18]</sup> has been investigated in ethylene glycol (EG) as a solvent. Systematic experiments have been performed, changing reaction times, temperatures, pH values and metal salts. The products and intermediates were synthesized in a microwave assisted polyol process, isolated and characterized by powder X-ray diffraction (PXRD), scanning electron microscopy (SEM), high resolution transmission electron microscopy (HR-TEM), scanning electron microscopy (SEM), energy-dispersive X-ray spectroscopy (EDS), high-pressure liquid chromatography coupled with mass spectrometry, UV-Vis spectroscopy, and Fourier transformed infrared spectroscopy (FT-IR).

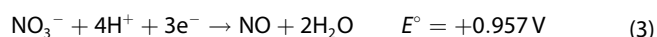
## 2. Results and Discussion

### 2.1. Reduction of Bi(NO<sub>3</sub>)<sub>3</sub> in EG

Considering the standard potentials of Bi<sup>3+</sup> and Ni<sup>2+</sup> in aqueous solutions (Equations 1 and 2), bismuth is generally more noble and therefore its cation is easier to reduce.<sup>[21]</sup> Although these values are in a strict sense only valid for aqueous systems, it is reasonable to assume, that the relative reduction behavior in polyols is comparable.



Additionally, reactions containing nitrate anions are prone to produce nitrous gases upon heating, which are then capable of reacting with the organic and inorganic intermediates (Equation 3):



Bismuth nitrate easily dissolves in EG resulting in a clear solution. As reported before, the centrosymmetric dinuclear complex [Bi(C<sub>2</sub>H<sub>5</sub>O<sub>2</sub>)(EG)(NO<sub>3</sub>)<sub>2</sub>]<sub>2</sub> can be crystallized from such solutions at ambient temperature,<sup>[22]</sup> which means that EG is deprotonated at ambient temperature without addition of a base.

To obtain information about the species present in solution, HPLC-MS measurements of dilute solutions of Bi(NO<sub>3</sub>)<sub>3</sub> in EG were performed at room temperature. A distinct signal can be observed for a dinuclear complex with two neutral EG ligands and one deprotonated ligand. The primary species, however, seems to be a mononuclear complex, with two deprotonated EG ligands. Apparently, the nitrate anions react with EG to produce HNO<sub>3</sub> (Figure S1 †), which is counterintuitive regarding the acid constants.

At around 180 °C, a greyish-white X-ray amorphous powder precipitates, which probably consist of a bismuth-glycolate coordination polymer. Raising the reaction temperature to 210 °C changes the color of the suspension to black, indicating the reduction of Bi<sup>3+</sup> to Bi<sup>0</sup>. According to powder X-ray diffraction, the resulting spherical particles have the crystal structure of the rhombohedral standard modification of bismuth. SEM images reveal a broad size distribution with diameter ranging from 50 nm to 250 nm. Size and shape of the particles depend on the reaction time and temperature. Without the addition of surfactants, reaction times up to 2 h lead to agglomeration of the particles. Considering the low melting point of bismuth of 271 °C, these reaction conditions may facilitate intra-particle sintering and partial melting of the particles, resulting in an almost perfect spherical shape.<sup>[23]</sup>

### 2.2. Reduction of Ni salts in EG

In general, nickel acetate, is reducible in polyols between 200 °C and 250 °C depending on additional promoting agents.<sup>[24]</sup> Ni(OAc)<sub>2</sub> slowly dissolves in EG resulting in a light green solution. UV-Vis spectroscopy of the solution shows a typical absorbance spectrum for octahedral complexes with a distinct band at 395 nm, attributed to the <sup>3</sup>A<sub>2g</sub>(F)→<sup>3</sup>T<sub>1g</sub>(P) transition, indicating a threefold complexation by EG, which is also in agreement with reported crystal structures.<sup>[22,25]</sup> Additional bands at 662 nm and 727 nm have been assigned to the <sup>3</sup>A<sub>2g</sub>(F)→<sup>3</sup>T<sub>1g</sub>(F) and <sup>3</sup>A<sub>2g</sub>(F)→<sup>3</sup>T<sub>2g</sub>(F) transitions respectively (Figure S2 †). We observed reduction of nickel acetate in EG only at temperatures exceeding 250 °C without addition of auxiliaries.

Nickel nitrate is easily soluble in EG yielding a light green solution. Analogously to nickel acetate, the solution contains octahedral complexes with identical UV-Vis bands. Additionally, the spectrum shows a characteristic band at 303 nm, which can be attributed to the nitrate ion (Figure S2 †).<sup>[26]</sup> To identify the predominant species in solution, HPLC-MS measurements were performed. Due to an increased affinity of the eluent acetonitrile towards nickel, some fractions, namely at 223 *m/z*, indicate a partial ligand exchange EG vs. acetonitrile during elution (Figure S3 †). Nevertheless, the overall tendency clearly leans toward mononuclear species in solution, being in agreement with the postulated and experimentally determined crystal structures.<sup>[22,27,28]</sup> The reduction behavior is different to that of nickel acetate, in that the necessary temperature to induce a quick reduction to Ni<sup>0</sup> exceeds 280 °C, which is in agreement with the slow formation of intermetallic compounds explained below.

Earlier studies reported, that NiCl<sub>2</sub>·6H<sub>2</sub>O is not reduced in EG unless strong reducing agents or NaOH were added to the solution.<sup>[29,30]</sup> Due to their strong Lewis base character, chloride anions tend to bind directly to Ni<sup>2+</sup>. Antti et al. reported the crystal structure of a compound that crystallized from a solution of NiCl<sub>2</sub> in EG, which contained the dinuclear complex [Ni<sub>2</sub>Cl<sub>2</sub>(EG)<sub>4</sub>]<sup>2+</sup> with bridging chlorido and chelating EG ligands in octahedral geometry as determined from UV-Vis spectra.<sup>[31]</sup> To determine the nickel-containing complexes in solution,

HPLC-MS measurements were performed (Figure S4†). The mass spectra show a clear signal for a species that has exactly the mass of this dinuclear complex, which suggests  $[\text{Ni}_2\text{Cl}_2(\text{EG})_4]^{2+}$  to be also the dominant species in solution. Apparently, the affinity of chloride towards  $\text{Ni}^{2+}$  causes the observed inertness against reduction by EG.

### 2.3. Reaction of $\text{Bi}(\text{NO}_3)_3$ with $\text{Ni}(\text{OAc})_2$

Upon heating a mixture of  $\text{Bi}(\text{NO}_3)_3$  and  $\text{Ni}(\text{OAc})_2$  in EG to temperatures between 210 °C and 240 °C by microwave irradi-

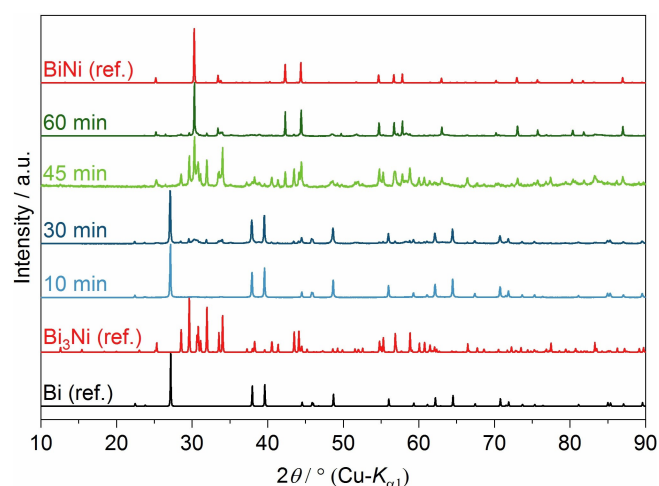


**Figure 1.** PXRD patterns of solid reaction products obtained from the reaction of  $\text{Ni}(\text{OAc})_2$  and  $\text{Bi}(\text{NO}_3)_3$  in EG at 250 °C after different reaction times. Bi (ref.), BiNi (ref.) and  $\text{Bi}_3\text{Ni}$  (ref.) are the calculated powder diagrams based on the crystal structure of Bi, BiNi and  $\text{Bi}_3\text{Ni}$  according to ICSD No. 64703, No. 410878 and No. 391336 respectively.

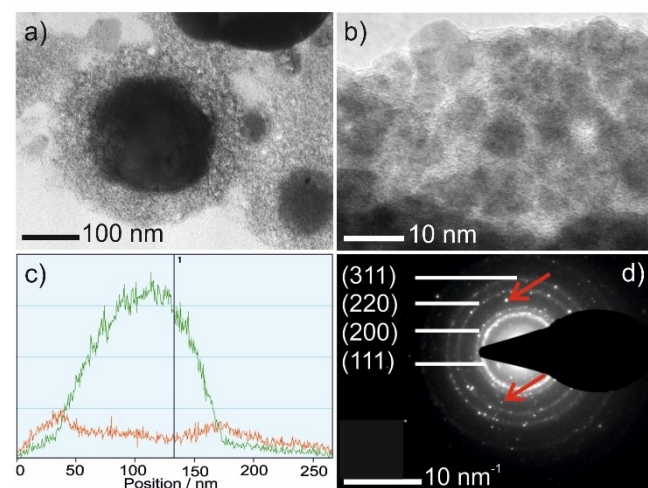


**Figure 2.** a) Images of Bi particle encased in a Ni nanoparticle shell (FIB slice) after 10 min reaction time. b) HR-TEM image of the shell showing individual crystalline particles. c) EDX line-scan indicating the elemental distribution of Bi (green) and Ni (red) across a random core-shell particle. d) Representative SAED pattern of the particle shell with Miller indices of Ni: red arrows pointing towards non-indexed reflections (For the SAED area see Figure S7†).

ation, the sole solid product obtained was bismuth according to PXRD, confirming that the reduction power of EG is not high enough to reduce  $\text{Ni}^{2+}$  to  $\text{Ni}^0$  (Figure S5†). At approx. 250 °C, the reaction slowly generated intermetallic phases (Figure 1). After 30 min, subtle and broad reflections in the range  $30^\circ \leq 2\theta \leq 35^\circ$  ( $\text{Cu-K}\alpha_1$ ) emerge alongside the dominating reflections of bismuth, which can be attributed to  $\text{Bi}_3\text{Ni}$ . After 45 min, the reflections of the  $\text{Bi}_3\text{Ni}$  phase are clearly visible. Additional distinct reflections, most obviously at  $2\theta = 30.3^\circ$ , are visible, which can be assigned to BiNi, while the reflections of elemental bismuth have completely vanished. The final product after approx. 60 min is an almost phase-pure BiNi powder, with minor  $\text{Bi}_3\text{Ni}$  impurities probably due to stoichiometric errors. Evidently, no traces of elemental nickel can be found in all samples.

To monitor the incorporation of nickel into the particles, HR-TEM images were recorded. The images revealed a shell around the spherical bismuth particles. Fixating the particles in epoxy resin and slicing them with a focused ion beam, uncovered the core-shell structure of the particles (Figure 2a), which, to the best of our knowledge, is the first reported spherical self-organized bismuth-nickel core-shell nanostructure. Previously reported core-shell structures were obtained by electrodeposition in a matrix.<sup>[32]</sup> The bismuth cores have a broad size distribution with diameters between 30 nm and 250 nm, whereas the nickel shell has a thickness between 50 nm and 250 nm. The shell consists of densely packed crystalline nanoparticles of 2 nm to 10 nm in diameter (Figure 2b). The composition of these particles was investigated by EDS, SAED, and STEM-mapping. EDS point analysis clearly identified nickel in the shell around the bismuth core. EDS line-scans across the particles exhibit an increased signal of nickel in the shell and a drop of intensity in the central part, which we interpret as a full encasement with Ni (Figure 2c). To determine the structure of the shell SAED measurements were performed (Figure 2d). The observed diffraction rings can clearly be assigned to the diffraction pattern of elemental nickel, especially for the lattice planes (111), (200), (220) and (311). Some non-indexed single reflections can probably be attributed to Bi or the newly formed  $\text{Bi}_3\text{Ni}$  in the interphase region. Apparently, the nickel nanoparticles did not provide any reflections in the PXRD measurements due to finite size effects. STEM mapping of sliced particles further corroborated the core-shell structure showing the clear distinction of a nickel shell and a bismuth core, displaying no mixing between the individual structures (Figure S6†).

Analysis of the surface chemistry by FT-IR measurements also revealed the existence of organic materials in the early stages of the reaction (Figure 3). Absorption bands were assigned to characteristic OH stretching at  $3360\text{ cm}^{-1}$  to  $3200\text{ cm}^{-1}$ , CH stretching at  $2930\text{ cm}^{-1}$  to  $2860\text{ cm}^{-1}$  and C-OH deformation modes at  $1300\text{ cm}^{-1}$  to  $1450\text{ cm}^{-1}$ . In comparison to pristine EG, the OH stretching band is slightly shifted towards lower energies and significantly reduced in intensity, which implies a partial deprotonation of the polyol and assumingly a coordination to the particle surfaces. The absorption band between  $1580\text{ cm}^{-1}$  and  $1640\text{ cm}^{-1}$ , which does not occur with

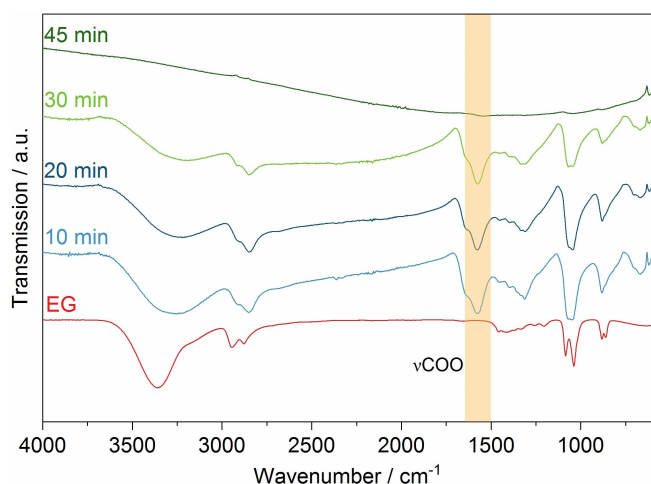


**Figure 3.** FT-IR spectra of powders obtained from the reaction of  $\text{Ni}(\text{OAc})_2$  and  $\text{Bi}(\text{NO}_3)_3$  in EG after different reaction times. The interval for the absorption band of a COO group (stretching mode) is highlighted.

pristine EG, can be attributed to COO stretching modes. These bands can be caused by acetate anions of the starting materials or by carboxylate anions resulting from the oxidation of EG. As this band also occurs in the reaction without acetate anions in the starting materials, oxidation products seem to be reasonable. We assume, that carboxylate anions are attached to the positively charged surface of the nickel particles and hold the shell together.<sup>[33]</sup> The absorption bands located at around  $1315\text{ cm}^{-1}$  are attributed to residues of nitrate anions. Towards the end of the reaction, the characteristic bands of the organic products almost disappear as the nickel shell slowly depletes (Figure S8a–c†). The respective IR spectra only show a wide-range absorption, which is typical for metallic samples.

Following these findings, we suggest, that,  $\text{Ni}^{2+}$  is reduced on the surface of previously formed bismuth particles, which act as nucleation sites for heterogeneous reduction. According to the nucleation theory, heterogeneous nucleation separates nucleation from particle growth, resulting in more or less monodisperse particles.<sup>[34]</sup> Furthermore, the higher nucleation rate increases the number of particles, which leads to a smaller diameter of the final particles.<sup>[35]</sup> Several TEM images corroborate this hypothesis, as only a few small nickel particles were found separated from the bismuth particles. After particle growth, a diffusion process begins at the interfaces. Since the concentration of elemental nickel in the bismuth particle is low at the beginning, the bismuth-rich phase  $\text{Bi}_3\text{Ni}$  is formed first, as has been shown by PXRD measurements. As the reaction proceeds, more nickel is incorporated, which leads to a mixture of  $\text{Bi}_3\text{Ni}$  in the inner regions and  $\text{BiNi}$  in the outer region of the particles. With respect to the observed sequence of product formation, it is reasonable to assume, that a nickel flux into the bismuth core is the predominant diffusion process. It might be based on the lower atomic mass and the smaller atomic radius of nickel ( $1.38\text{ \AA}$ ) compared to bismuth ( $1.70\text{ \AA}$ ).<sup>[36]</sup> We also do not observe hollow product particles that would be expected if bismuth was the mobile partner. Nonetheless, the vicinity of

the reaction temperature to the melting point of bismuth fosters the diffusion and formation of the intermetallic phases.

#### 2.4. Verification of the Solid-State Diffusion Mechanism

To obtain additional information on the proposed diffusion mechanism in the solid, the individual steps in the reaction were emulated (Figure 4). In a first step, the reduction of bismuth was separated from the process. Bismuth particles were prepared (for details, see experimental section) and immediately re-suspended in EG. After adding  $\text{Ni}(\text{OAc})_2$  the suspension was heated to  $250^\circ\text{C}$  for 60 min. This reaction yielded almost pure  $\text{BiNi}$  powder with small residues of  $\text{Bi}_3\text{Ni}$ . This proves that simultaneous reduction of the two metals is not essential and is in line with the idea of bismuth particles acting as nucleation sites for nickel nanoparticles. As reaction temperatures below  $250^\circ\text{C}$  yield no intermetallic compound a direct reaction of  $\text{Ni}(\text{OAc})_2$  with Bi is unlikely, see above.

The solid-state reaction of  $\text{Bi}_3\text{Ni}$  with addition nickel to  $\text{BiNi}$  was reproduced starting from freshly produced  $\text{Bi}_3\text{Ni}$  particles and  $\text{Ni}(\text{OAc})_2$ . Despite the considerable difference between the melting point of  $\text{Bi}_3\text{Ni}$  ( $467^\circ\text{C}$ ) and the applied reaction temperature of  $250^\circ\text{C}$ , phase-pure  $\text{BiNi}$  was formed, confirming the diffusion of in-situ formed nickel into the  $\text{Bi}_3\text{Ni}$  particles.

In order to assess the importance of direct contact between bismuth and locally formed nickel particles, particles of both elements were produced separately and then dispersed together in EG. After 60 min at  $250^\circ\text{C}$ , the solid product was a mixture of bismuth and  $\text{Bi}_3\text{Ni}$  with small amounts of  $\text{BiNi}$  and nickel. There are two aspects that make a difference. On the one hand, nickel particles obtained from a standard polyol process have diameters between 100 nm and 200 nm, which is 10 to 20 times larger than the particles observed in the nickel shell of our bismuth-nickel core-shell particles. The time to consume such

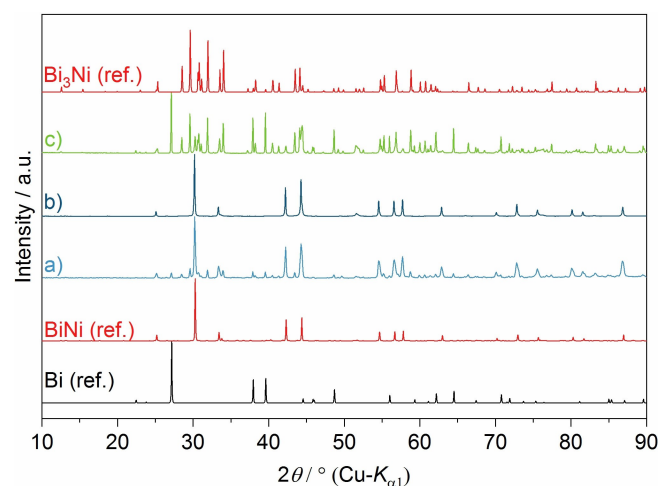


**Figure 4.** PXRD patterns of products obtained after reacting a) bismuth particles with  $\text{Ni}(\text{OAc})_2$ , b)  $\text{Bi}_3\text{Ni}$  particles with  $\text{Ni}(\text{OAc})_2$  and c) bismuth particles with nickel particles in EG at  $250^\circ\text{C}$  for 1 h. Bi (ref.),  $\text{BiNi}$  (ref.) and  $\text{Bi}_3\text{Ni}$  (ref.) are the calculated powder diagrams based on the crystal structure of Bi,  $\text{BiNi}$  and  $\text{Bi}_3\text{Ni}$  according to ICSD No. 64703, No. 410878 and No. 391336 respectively.



large nickel particles is much longer. On the other hand, effective collisions must occur between the two types of freely dispersed particles to allow reaction. Additionally, the more nickel is used up, the longer it takes for a free nickel particle to successfully collide with a suitable reaction partner. Hence, for a fast and quantitative formation of the intermetallic phases, the heterogeneous reduction of nickel on the surface of bismuth particles is crucial.

## 2.5. Effects of Temperature and pH in the Reaction of $\text{Bi}(\text{NO}_3)_3$ and $\text{Ni}(\text{OAc})_2$

Diffusion can be actively promoted by raising the temperature of the system leading to an increased mobility in the solid, which facilitates the incorporation of nickel in the bismuth core.<sup>[37]</sup> Hence, the reaction temperature was raised to 260 °C and 270 °C respectively, which accelerated the reaction immensely (Figure 5). At 260 °C, the BiNi phase is almost completely formed within 30 min, yet residues of  $\text{Bi}_3\text{Ni}$  are detectable. Raising the reaction temperature to 270 °C yields phase-pure BiNi powder in probably less than 30 min. In addition to the accelerated diffusion, elevated temperatures increase the reduction power of EG, which leads to higher nucleation rates. As mentioned before, higher nucleation rates produce smaller particles, which directly affects the time for particle to be consumed in the follow-up diffusion-controlled reaction.

The pH has a substantial effect on the reduction power of the polyol. A base added to the reaction solution is able to deprotonate the alcohol group to generate alkoxides, which have a higher electron density and a higher affinity to coordinate the metal ions than the alcohol. Theoretical studies postulated that hydroxide anions further deprotonate the  $\alpha$ -carbon of the alkoxide ligand, which leaves two electrons for the reduction of the metal cation.<sup>[38]</sup> It was observed that the

formation of small particles is favored in the presence of hydroxide ions, which increases the diffusion rate in subsequent reactions.<sup>[24,39]</sup> Hence, a high pH improves the reaction kinetics, leading to shorter reaction times.

The reaction of  $\text{Bi}(\text{NO}_3)_3$  with  $\text{Ni}(\text{OAc})_2$  using NaOH to tune the pH value was monitored by PXRD measurements of the intermediate products (Figure 6). Overall, the reaction follows the same scheme as under neutral conditions. The first observable solid phase is elemental Bi. In contrast to the reaction without base, the intermetallic compound  $\text{Bi}_3\text{Ni}$  emerges quicker, confirming promoted nickel reduction.<sup>[40]</sup> The retention time of newly formed  $\text{Bi}_3\text{Ni}$  is noticeably long. Seemingly, the faster production of nickel leads to a quicker onset of  $\text{Bi}_3\text{Ni}$  formation, but the diffusion rate in the solid is unchanged, making it the rate limiting factor. Nonetheless, the final phase BiNi is achieved faster than in neutral media (45 min vs. 60 min), which confirms the promoting effect of the added base. One can conclude that for the reaction of bismuth nitrate with nickel acetate, the temperature has a higher impact on the reaction kinetics than the addition of NaOH.

The influence of the basicity of the solution is also seen if  $\text{Bi}(\text{OAc})_3$  and  $\text{Ni}(\text{OAc})_2$  are reacted in EG. This reaction generally shows a slightly shorter reaction time compared to the  $\text{Bi}(\text{NO}_3)_3/\text{Ni}(\text{OAc})_2$  mixture due to the increased number of acetate anions in solution. FT-IR measurements display a full deprotonation of EG, which leads to a higher affinity towards nickel and results in a higher reduction power. (Figure S9 and S10†)

## 2.6. Reaction of $\text{Bi}(\text{NO}_3)_3$ with $\text{Ni}(\text{NO}_3)_2$

To compare the reaction behavior of different nickel salts and to investigate the impact of the anion on the reaction kinetics, we also analyzed the reaction of  $\text{Bi}(\text{NO}_3)_3$  with  $\text{Ni}(\text{NO}_3)_2$  instead of  $\text{Ni}(\text{OAc})_2$ . The overall reaction conditions remained the same.

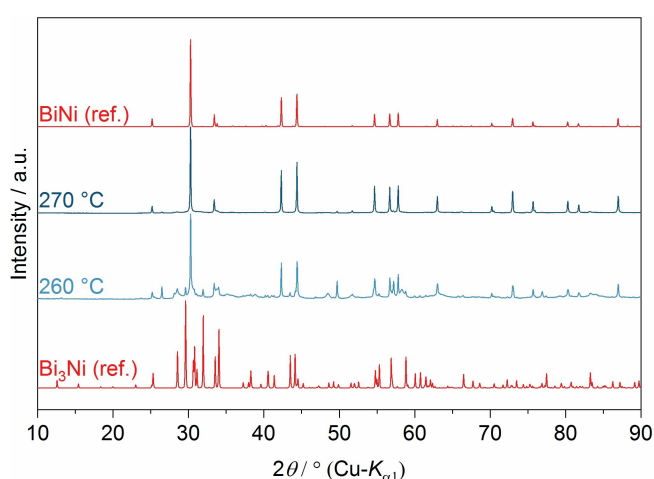


**Figure 5.** PXRD patterns of solid reaction products obtained from the reaction of  $\text{Ni}(\text{OAc})_2$  and  $\text{Bi}(\text{NO}_3)_3$  in EG after 30 min at higher reaction temperatures. BiNi (ref.) and  $\text{Bi}_3\text{Ni}$  (ref.) are the calculated diagrams based on the crystal structure of BiNi and  $\text{Bi}_3\text{Ni}$  according to ICSD No. 410878 and No. 391336 respectively.

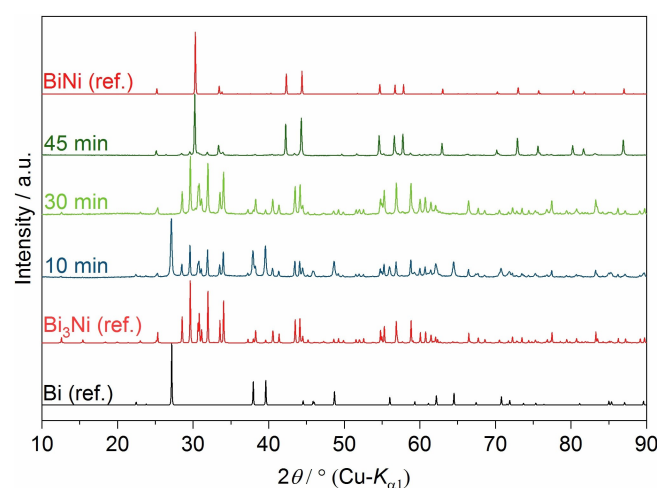


**Figure 6.** PXRD patterns of solid reaction products obtained from the reaction of  $\text{Ni}(\text{OAc})_2$  and  $\text{Bi}(\text{NO}_3)_3$  in EG at 250 °C in alkaline solution after different reaction times. Bi (ref.), BiNi (ref.) and  $\text{Bi}_3\text{Ni}$  (ref.) are the calculated diagrams based on the crystal structure of Bi, BiNi and  $\text{Bi}_3\text{Ni}$  according to ICSD No. 64703, No. 410878 and No. 391336 respectively.

The obtained intermediates were collected and analyzed by PXRD measurements (Figure 7).

The progress of the reaction is similar to the reaction of  $\text{Bi}(\text{NO}_3)_3$  with  $\text{Ni}(\text{OAc})_2$  although with strongly decreased kinetics. The reducibility of nickel cations in the pure nitrate system is lowered in comparison to a system containing also acetate as mentioned before due to the higher reduction temperature of  $\text{Ni}(\text{NO}_3)_3$ . These findings corroborate our recent results on mono-metallic systems, showing a dependency of the reducibility on the counter anion. A detailed description of this reaction can be found in the SI.

Analysis of the surface chemistry by FT-IR measurements revealed major differences in oxidation products compared to the reaction with  $\text{Ni}(\text{OAc})_2$  (Figure 8). Strikingly, the OH stretching band at  $3400\text{ cm}^{-1}$  to  $3200\text{ cm}^{-1}$  and the otherwise concise CH stretching bands at  $2930\text{ cm}^{-1}$  to  $2860\text{ cm}^{-1}$  are

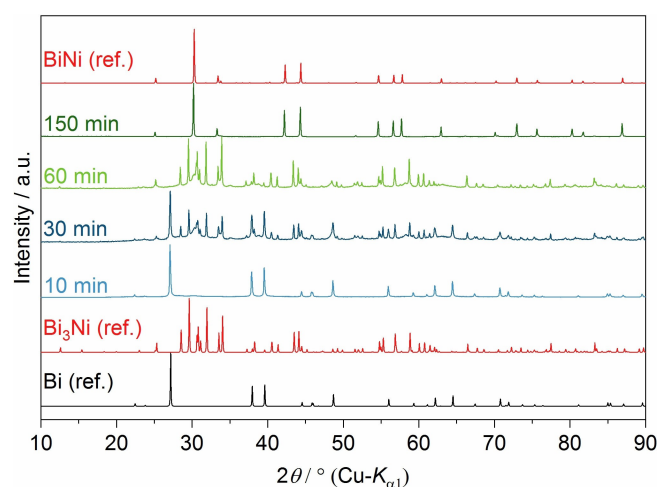


**Figure 7.** PXRD patterns of the solid reaction products obtained from the reaction of  $\text{Ni}(\text{NO}_3)_3$  and  $\text{Bi}(\text{NO}_3)_3$  in EG at  $250^\circ\text{C}$  after different reaction times. Bi (ref.), BiNi (ref.) and  $\text{Bi}_3\text{Ni}$  (ref.) are the calculated diagrams based on the crystal structure of Bi, BiNi and  $\text{Bi}_3\text{Ni}$  according to ICSD No. 64703, No. 410878 and No. 391336 respectively.

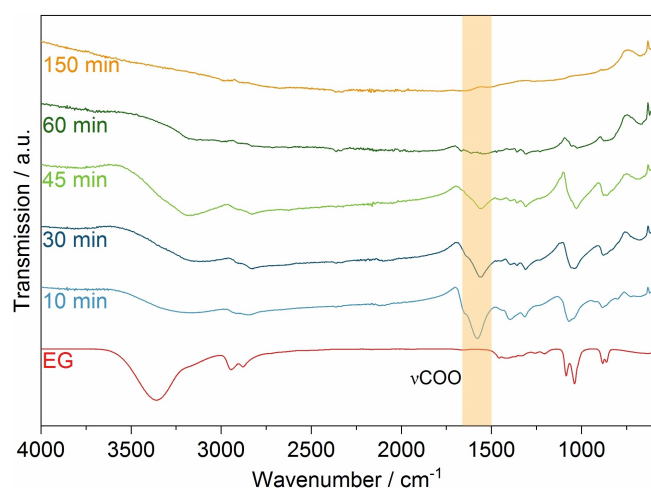


**Figure 8.** FT-IR spectra of powders obtained from the reaction of  $\text{Ni}(\text{NO}_3)_3$  and  $\text{Bi}(\text{NO}_3)_3$  in EG after different reaction times. The interval for the absorption band of a COO group (stretching mode) is highlighted.

almost undetectable for all collected intermediates at  $250^\circ\text{C}$ . The residual OH stretching band may emerge from left over EG or absorbed water on the surface. Additionally, an intensive COO stretching band at  $1575\text{ cm}^{-1}$  occurs, which indicates an oxidation of EG. Taking both observations into consideration, a complete oxidation of EG to oxalate is very likely due to a secondary redox reaction between the second alcohol group and the nitrate anion, which additionally leads to the formation of nitrous gases – indicated by the brownish color of the solution – according to Equation 3. After 60 min, almost no IR bands are visible any more in range between  $4000\text{ cm}^{-1}$  and  $1200\text{ cm}^{-1}$  indicating that no oxidation products are bond to the surface of the intermediates. The final product exhibits a broad absorption resulting from the metallic character of the BiNi particles. Seemingly, no organic molecules are attached to the particles after the reaction has finished.

## 2.7. Effect of Temperature and pH in the Reaction of $\text{Ni}(\text{NO}_3)_3$ and $\text{Bi}(\text{NO}_3)_3$

Using a temperature of  $260^\circ\text{C}$  instead of  $250^\circ\text{C}$  resulted in a significant shortening of the reaction time due to increased reduction and diffusion rates (Figure 9). Yet, the reaction proceeds noticeably slower than reactions with  $\text{Ni}(\text{OAc})_2$ , again confirming the dependency of the reduction rate on the anion type. Alkaline conditions have the same effects as in reactions with  $\text{Ni}(\text{OAc})_2$ , as after 60 min virtually pure BiNi is obtained (Figure 10). Considering the reaction times to achieve a full conversion, the alkaline conditions have a slightly stronger effect on the nitrate system than elevated temperatures.

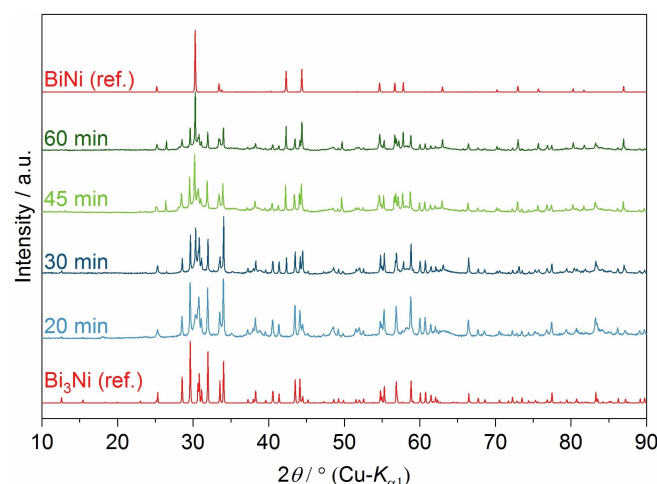


**Figure 9.** PXRD patterns of the solid reaction products obtained from the reaction of  $\text{Ni}(\text{NO}_3)_3$  and  $\text{Bi}(\text{NO}_3)_3$  after different reaction times at  $260^\circ\text{C}$ . BiNi (ref.) and  $\text{Bi}_3\text{Ni}$  (ref.) are the calculated diagrams based on the crystal structure of BiNi and  $\text{Bi}_3\text{Ni}$  according to ICSD No. 410878 and No. 391336 respectively.

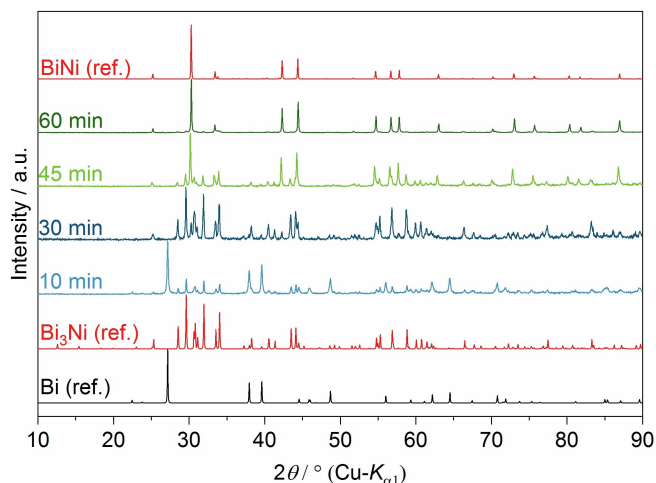


**Figure 10.** PXRD patterns of the solid reaction products obtained from the reaction of  $\text{Ni}(\text{NO}_3)_2$  and  $\text{Bi}(\text{NO}_3)_3$  in EG at  $250^\circ\text{C}$  after different reaction times in alkaline solution. Bi (ref.), BiNi (ref.) and  $\text{Bi}_3\text{Ni}$  (ref.) are the calculated diagrams based on the crystal structure of Bi, BiNi and  $\text{Bi}_3\text{Ni}$  according to ICSD No. 64703, No. 410878 and No. 391336 respectively.

## 2.8. Reaction of $\text{Bi}(\text{NO}_3)_3$ with $\text{NiCl}_2$ and $\text{NiBr}_2$

As expected, reacting  $\text{Bi}(\text{NO}_3)_3$  and  $\text{NiCl}_2$  in EG at  $250^\circ\text{C}$  yielded no intermetallic particles but only elemental bismuth. Interestingly, prior to the reduction of  $\text{Bi}^{3+}$  a brown solid precipitated. The precipitate was identified as BiOCl by PXRD (Figure 11), which crystallized in thin platelets of different size in the micron and submicron range with smooth surfaces (Figure S11a†). The brown color of the precipitate (BiOCl is colorless) is probably caused by finely dispersed nanoparticles of bismuth. The reduction of BiOCl proceeds at  $220^\circ\text{C}$  and occurs directly at the surface of the platelets, which can be seen by the cleavage and roughening of the surface and the formation of small spheres

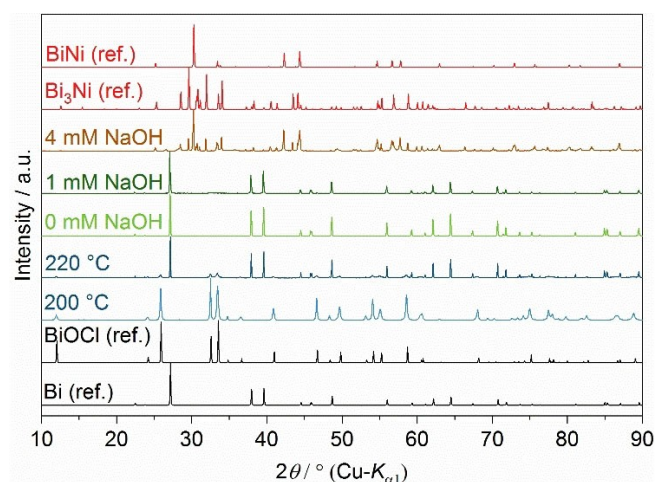
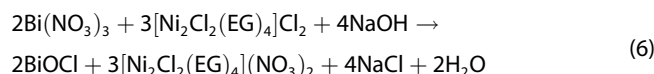
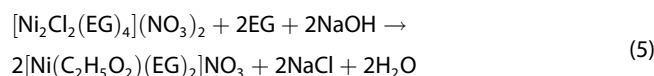
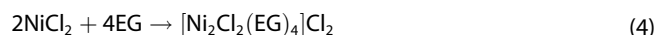


**Figure 11.** PXRD patterns of solid products obtained from the reaction of  $\text{NiCl}_2$  and  $\text{Bi}(\text{NO}_3)_3$  in EG at various temperatures and NaOH concentrations. Reactions with declared NaOH concentrations were performed at  $250^\circ\text{C}$  for 1 h. Bi (ref.), BiOCl (ref.), BiNi (ref.) and  $\text{Bi}_3\text{Ni}$  (ref.) are the calculated diagrams based on the crystal structure of Bi, BiOCl, BiNi and  $\text{Bi}_3\text{Ni}$  according to ICSD No. 64703, No. 195115 No. 410878 and No. 391336 respectively.

on it (Figure S11b†). PXRD patterns of the isolated powder after  $220^\circ\text{C}$  display strong reflections of elemental bismuth and some weak BiOCl reflections (Figure 11).

The pH seemingly plays an important role in the reduction process and therefore NaOH was added in a molar ratio of  $\text{Bi}^{3+} : \text{Ni}^{2+} : \text{OH}^- = 1:1:2$ . Again, BiOCl formed as an intermediate, which was then partly reduced to bismuth, but no intermetallic phase was obtained at  $250^\circ\text{C}$ . Increasing the NaOH concentration to 1:1:8 resulted in a mixture of  $\text{Bi}_3\text{Ni}$  and BiNi after 60 min at  $250^\circ\text{C}$  (Figure 11). This suggests that substantial deprotonation of EG is needed for the reduction of the stable  $[\text{Ni}_2\text{Cl}_2(\text{EG})_4]^{2+}$  complex.

In conclusion, we propose the following reaction mechanism:



Dissolving  $\text{NiCl}_2$  in EG leads to the dinuclear complex  $[\text{Ni}_2\text{Cl}_2(\text{EG})_4]^{2+}$  (Equation 4). Due to alkaline conditions, EG is deprotonated generating the alkoxide, which breaks the dinuclear complex and abstracts chloride from  $\text{Ni}^{2+}$  (Equation 5). Upon heating to approximately  $180^\circ\text{C}$ , BiOCl precipitates (Equation 6). Further heating induces the reduction of the mononuclear  $[\text{Ni}(\text{C}_2\text{H}_5\text{O}_2)(\text{EG})_2]^+$  complex, resulting in elemental nickel and nitrous gases, as described in Equation 3.

$\text{NiBr}_2$  shows a similar reaction behavior as  $\text{NiCl}_2$ , however, the addition of NaOH is not a necessity in this case. This can be rationalized by the weaker nucleophilicity of bromide compared to chloride, which leads to the formation of a homoleptic nickel complex with only EG ligands. A crystalline precipitate was obtained by dissolving  $\text{NiBr}_2$  in EG at  $70^\circ\text{C}$  and subsequent slow cooling to room temperature. The monoclinic crystals consist of a mononuclear species  $[\text{Ni}(\text{EG})_3]\text{Br}_2$ , in which  $\text{Ni}^{2+}$  is six-fold coordinated by three bidentate EG ligands without any bridging halide atoms (Figure 12), corroborating the hypothesis formulated in Equation 6.

Upon heating the reaction mixture of  $\text{NiBr}_2$  and  $\text{Bi}(\text{NO}_3)_3$  in EG, BiOBr precipitates at around  $180^\circ\text{C}$ . Increasing the reaction

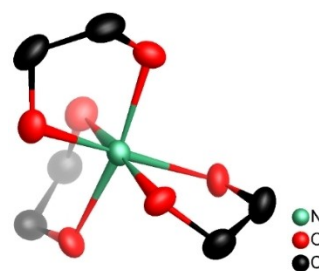


**Figure 12.** Molecular structure of the complex  $[\text{Ni}(\text{EG})_3]^{2+}$ . Hydrogen atoms are omitted for clarity. Ellipsoids comprise 90% of the probability density.

temperature to 250 °C for 30 minutes yielded a mixture of Bi<sub>3</sub>Ni and Bi (Figure 13). In the absence of Bi(NO<sub>3</sub>)<sub>3</sub>, NiBr<sub>2</sub> cannot be reduced at this temperature. To test whether this effect has to be attributed to bismuth or nitrate, the previously obtained BiOBr was used as a bismuth source, with otherwise unchanged reaction conditions. After 60 min of reaction, the PXRD revealed reflections of bismuth only, without any traces of elemental nickel or nickel containing compounds (Figure S12 †). Obviously, the presence of nitrate is essential for the reduction of NiBr<sub>2</sub>.

### 3. Conclusions

Systematic experiments were carried out to study the reaction mechanism of the formation of intermetallic phases in the binary system bismuth-nickel and the dependency on the nickel precursor, the temperature, pH value and anion type. The process involves consecutive reduction of bismuth and nickel cations. Herein, the nickel cations are most likely reduced on the surface of the bismuth particles, forming a hitherto unknown self-organized spherical core-shell structure, which is linked by the oxidation products of EG. Thereupon, a diffusion process is responsible for the generation of the intermetallic phases. The bismuth-rich phase Bi<sub>3</sub>Ni is formed first, as nickel diffuses into the bismuth core. After prolonged reaction times, the final BiNi phase is achieved and the nickel shell is lost. In the case of nickel acetate, EG is oxidized to acetate, whereas nickel nitrate induces a secondary redox reaction, where nitrate is reduced to NO, while oxidizing the pre-formed acetate to an oxalate. The overall kinetics are significantly promoted by either increasing the reaction temperature or the pH value. Increasing the temperature leads to a slightly increased reduction rate and a high increase in diffusion rate. Under alkaline conditions, the reduction rate is significantly increased, leading to faster onset of intermetallic phase formation. In accordance with previous

findings, nickel nitrate is harder to be reduced than nickel acetate,<sup>[41]</sup> but the overall reaction mechanism seems unchanged. Nickel halides, however, introduce a different reaction mechanism, as they need a suitable anion at the bismuth cation to perform an anion exchange. The exchange leads to the formation of bismuth oxide halides and easily reducible nickel species. The subsequent phase formation then follows the previous reaction pattern. Nickel chloride poses a special case due to the formation of a dinuclear complex species in solution. The reaction needs a very high concentration of NaOH to produce enough alkoxides in order to break the bridging bonds in this complex. In general, the reducibility can be ordered as  $\text{AcO}^- > \text{NO}_3^- > \text{Br}^- > \text{Cl}^-$ .

## Experimental Section

### Chemicals

Ethylene glycol (Fluka 99.5%) was used as received. Hydrated nickel (II) and bismuth(III) salts were used for all syntheses: Ni(OAc)<sub>2</sub>·4H<sub>2</sub>O (Merck, 99%), Ni(NO<sub>3</sub>)<sub>2</sub>·6H<sub>2</sub>O (Riedel-de Haën, 98%), NiCl<sub>2</sub>·6H<sub>2</sub>O (Grüssing, 98%). NiBr<sub>2</sub>·3H<sub>2</sub>O (Alfa Aesar, 98%), Bi(NO<sub>3</sub>)<sub>3</sub>·5H<sub>2</sub>O (VWR, 98%). For some experiments, solutions of NaOH (Grüssing, 99%) in EG with a concentration of 1 mol l<sup>-1</sup> was used. For FIB lamella preparation G1 epoxy resin (Gatan) and carbon nanoparticles (Vulcan XC 72, 25–75 nm) were used.

### Synthesis

All experiments were performed in a microwave-assisted polyol process in a CEM Discover SP synthesis and were carried out in 35 mL Pyrex® vessels equipped with magnetic stirring bars ensuring proper mixing of the reagents. All reaction mixtures were heated to the desired temperature within 4 min by using microwave radiation. For each synthesis, the respective bismuth and nickel compounds (0.5 mmol) were mixed with 10 ml of EG. In case of addition of 1 mol l<sup>-1</sup> NaOH solution, less EG was added to keep the reaction volume of 10 ml. Bismuth particles were obtained by dissolving 1 mmol of Bi(NO<sub>3</sub>)<sub>3</sub>·5H<sub>2</sub>O in 10 ml of EG. The mixture was heated to 220 °C for 10 min. Nickel particles were obtained by dissolving 1 mmol of Ni(OAc)<sub>2</sub>·4H<sub>2</sub>O in 10 ml of EG. The mixture was heated to 250 °C for 10 min. Bi<sub>3</sub>Ni particles were obtained by mixing 1.5 mmol of Bi(NO<sub>3</sub>)<sub>3</sub>·5H<sub>2</sub>O and 0.5 mmol of Ni(OAc)<sub>2</sub>·4H<sub>2</sub>O in 9 ml of EG and 1 ml of 1 mol l<sup>-1</sup> NaOH solution. The mixture was heated to 250 °C for 30 min. After the adjusted reaction time, the vessel was cooled with a stream of air to 60 °C inside the microwave device and then removed. The black powdery products were isolated by centrifugation at 4400 rpm, washed several times with 5–10 mL of ethanol or acetone to remove residual solvent, and dried overnight under vacuum at room temperature.

### Preparation of [Ni(EG<sub>3</sub>)]Br<sub>2</sub> Crystals

The crystals were prepared by dissolving NiBr<sub>2</sub>·3H<sub>2</sub>O (1.9 g, 7 mmol) in 2 ml of EG at 70 °C. Afterwards, the dark green solution was slowly cooled down to room temperature and stored at 4 °C. After one week plate-like crystals were visible.

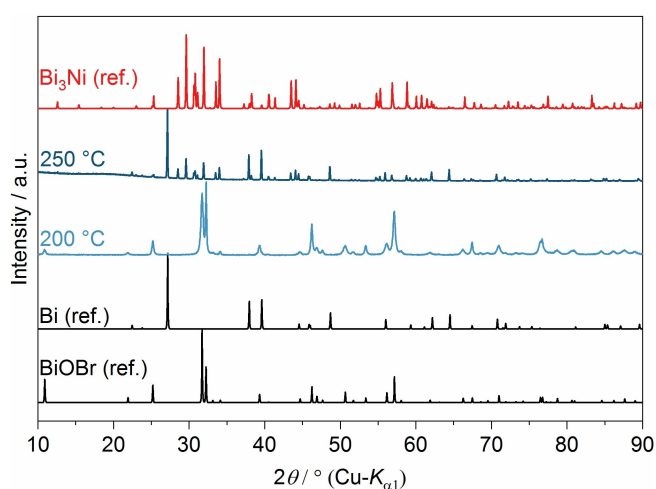


**Figure 13.** PXRD patterns of solid products obtained from the reaction of NiBr<sub>2</sub> and Bi(NO<sub>3</sub>)<sub>3</sub> in EG after 30 min at different reaction temperatures. Bi (ref.), BiOBr (ref.) and Bi<sub>3</sub>Ni (ref.) are the calculated diagrams based on the crystal structure of Bi, BiOBr and Bi<sub>3</sub>Ni according to ICSD No. 64703, No. 61225, No. 410878 and No. 391336 respectively.



## Preparation of FIB Lamellae

The epoxy resin was mixed with the carbon nanoparticles and the reaction products until a pulpy mixture was obtained, which then was hardened overnight at 80 °C at ambient pressure conditions. The lamellae were achieved with a FIB Helios NanoLab 600i (FEI) using gallium ions at a voltage of max. 30 kV. Afterwards, the lamellae were transferred onto copper grids and fixed by platinum ion deposition before they were transferred into the HR-TEM.

## Powder Characterization

PXRD patterns were recorded at 296(1) K with an X'Pert Pro MPD diffractometer (PANalytical) equipped with a curved Ge(111) monochromator by using Cu-K $\alpha_1$  radiation ( $\lambda = 1.54056 \text{ \AA}$ ). The powder diagrams of Bi (deposition number CSD-64703), Bi<sub>3</sub>N (CSD-391336), BiNi (CSD-410878), BiOCl (CSD-195115) and BiOBr (CSD-61225) used as references have been calculated from single crystal structure data deposited in the ICSD<sup>[42]</sup> Fourier-transform infrared (FT-IR) spectra were measured with a Vertex 80 (Bruker) spectrometer in attenuated total reflectance mode in the wavelength range 4000–600 cm<sup>-1</sup>. Scanning electron microscopy (SEM) was performed using a SU8020 electron microscope (Hitachi) equipped with a triple-detector system for secondary and low-energy back-scattered electrons with an acceleration voltage of 2 kV. For high resolution transmission electron microscopy (HR-TEM) and selected area electron diffraction (SAED), energy-dispersive X-ray spectroscopy (EDX) and scanning transmission electron microscopy (STEM) a Tecnai G2 (FEI) with an acceleration voltage of 200 kV and a LaB<sub>6</sub> filament was used. Ultraviolet-visible light spectroscopy was performed in double beam mode on a Cary 4000 (Bruker) in standard quartz glass cuvettes. High pressure liquid chromatography coupled with mass spectrometry (HPLC-MS) was carried out on 1260 Infinity II LC system (Agilent Technologies) coupled with a G6538 A mass spectrometer (Agilent Technologies) measuring with a scan rate of 1 s<sup>-1</sup>.

## Single-Crystal X-Ray Crystallography

A suitable crystal of [Ni(EG)<sub>3</sub>]Br<sub>2</sub> was mounted in a cryo-loop and cooled to 262 K under flowing nitrogen gas. Intensity data were collected with a four-circle diffractometer Kappa Apex2 (Bruker) equipped with a CCD- detector using graphite-monochromated Mo-K $\alpha$  radiation ( $\lambda = 0.71073 \text{ \AA}$ ). Data were corrected for Lorentz and polarisation factors,<sup>[43]</sup> and multi-scan absorption correction<sup>[44]</sup> was applied. The structure was solved using SHELXT intrinsic phasing<sup>[45]</sup> and refined with full-matrix least-squares based on F<sub>o</sub><sup>2</sup> with SHELXL<sup>[46]</sup> using the OLEX2<sup>[47]</sup> program package. Refinement included anisotropic displacement parameters for all non-hydrogen atoms. Hydrogen atoms were refined with riding coordinates and displacement parameters. Graphics were developed with Diamond.<sup>[48]</sup> The crystal structure data have been deposited at the Cambridge Crystallographic Data Centre under deposition number CCDC-2008015

## Acknowledgements

We thank Almut Pöhl (Leibniz Institute for Solid State and Materials Research, Dresden) for preparation of FIB lamella. We also thank Susanne Goldberg (Faculty of Chemistry and Food Chemistry, TU Dresden) for TEM images, and Dr. Susanne Machill and Frank Drescher (Faculty of Chemistry and Food Chemistry, TU Dresden) for their help with HPLC-MS measurements. This work

was financially supported by the Deutsche Forschungsgemeinschaft (project-id 413437826).

## Conflict of Interest

The authors declare no conflict of interest.

**Keywords:** intermetallic phases · nanoparticles · polyol processes · microwave assisted synthesis · reduction reactions

- [1] A. Dasgupta, R. M. Rioux, *Catal. Today* **2018**, *330*, 2–15.
- [2] J. Rick, M.-C. Tsai, B. Hwang, *Nanomaterials* **2015**, *6*, 5.
- [3] M. Armbrüster, *Sci. Technol. Adv. Mater.* **2020**, *21*, 303–322.
- [4] Y. Yan, J. S. Du, K. D. Gilroy, D. Yang, Y. Xia, H. Zhang, *Adv. Mater.* **2017**, *29*, 1605997.
- [5] G. Sharma, A. Kumar, S. Sharma, M. Naushad, R. Prakash Dwivedi, Z. A. ALothman, G. T. Mola, *J. King Saud Univ. Sci.* **2019**, *31*, 257–269.
- [6] J. Li, S. Sun, *Acc. Chem. Res.* **2019**, *52*, 2015–2025.
- [7] A. Tavakoli, M. Sohrabi, A. Kargari, *Chem. Pap.* **2007**, *61*, 151–170.
- [8] F. Fievet, J. P. Lagier, B. Blin, B. Beaudoin, M. Figlarz, *Solid State Ionics* **1989**, *32–33*, 198–205.
- [9] H. Dong, Y. C. Chen, C. Feldmann, *Green Chem.* **2015**, *17*, 4107–4132.
- [10] T. S. Rodrigues, M. Zhao, T. H. Yang, K. D. Gilroy, A. G. M. da Silva, P. H. C. Camargo, Y. Xia, *Chem. Eur. J.* **2018**, *24*, 16944–16963.
- [11] F. Bonet, C. Guéry, D. Guyomard, R. Herrera Urbina, K. Tekaia-Elhsissen, J.-M. M. Tarascon, *Int. J. Inorg. Mater.* **1999**, *1*, 47–51.
- [12] K. J. Lee, Y. Il Lee, I. K. Shim, B. H. Jun, H. J. Cho, J. W. Joung, *Solid State Phenom.* **2007**, *124–126*, 1189–1192.
- [13] J. Teichert, M. Heise, J. H. Chang, M. Ruck, *Eur. J. Inorg. Chem.* **2017**, *2017*, 4930–4938.
- [14] M. Heise, J. H. Chang, R. Schönmann, T. Herrmannsdörfer, J. Wosnitza, M. Ruck, *Chem. Mater.* **2014**, *26*, 5640–5646.
- [15] R. Boldt, A. Grigas, M. Heise, T. Herrmannsdörfer, A. Isaeva, S. Kaskel, D. Köhler, M. Ruck, R. Skrotzki, J. Wosnitza, *Z. Anorg. Allg. Chem.* **2012**, *638*, 2035–2043.
- [16] N. L. Henderson, R. E. Schaak, *Chem. Mater.* **2008**, *20*, 3212–3217.
- [17] R. E. Cable, R. E. Schaak, *Chem. Mater.* **2005**, *17*, 6835–6841.
- [18] B. M. Leonard, R. E. Schaak, *J. Am. Chem. Soc.* **2006**, *128*, 11475–11482.
- [19] A. J. Biacchi, R. E. Schaak, *ACS Nano* **2011**, *5*, 8089–8099.
- [20] R. Boldt, A. Grigas, M. Heise, T. Herrmannsdörfer, A. Isaeva, S. Kaskel, D. Köhler, M. Ruck, R. Skrotzki, J. Wosnitza, *Z. Anorg. Allg. Chem.* **2012**, *638*, 2035–2043.
- [21] D. R. Lide, *CRC Handbook of Chemistry and Physics*, CRC Press, Raton, FL, **2005**.
- [22] J. Teichert, M. Ruck, *Eur. J. Inorg. Chem.* **2019**, *2019*, 2267–2276.
- [23] C. Goia, E. Matijević, D. V. Goia, *J. Mater. Res.* **2005**, *20*, 1507–1514.
- [24] T. Hinotsu, B. Jayadevan, C. N. Chinnasamy, K. Shinoda, K. Tohji, *J. Appl. Phys.* **2004**, *95*, 7477–7479.
- [25] E. González, A. Rodrigue-Witchel, C. Reber, *Coord. Chem. Rev.* **2007**, *251*, 351–363.
- [26] K. S. Krishnan, A. C. Guha, *Proc. Indian Acad. Sci. Sect. A* **1934**, *1*, 242–249.
- [27] A. Grün, E. Boedecker, *Ber. Dtsch. Chem. Ges.* **1910**, *43*, 1051–1062.
- [28] D. Knetsch, W. L. Groeneveld, *Inorg. Chim. Acta* **1973**, *7*, 81–87.
- [29] S. H. Wu, D. H. Chen, *J. Colloid Interface Sci.* **2003**, *259*, 282–286.
- [30] G. G. Couto, J. J. Klein, W. H. Schreiner, D. H. Mosca, A. J. A. de Oliveira, A. J. G. Zabin, *J. Colloid Interface Sci.* **2007**, *311*, 461–468.
- [31] B.-M. Antti, *Acta Chem. Scand.* **1975**, *29a*, 76–88.
- [32] Y. Jia, D. Yang, B. Luo, S. Liu, M. O. Tade, L. Zhi, *Nanoscale Res. Lett.* **2012**, *7*, 130.
- [33] Z. Libor, Q. Zhang, *Mater. Chem. Phys.* **2009**, *114*, 902–907.
- [34] V. K. LaMer, A. S. Kenyon, *J. Colloid Sci.* **1947**, *2*, 257–264.
- [35] F. Fievet, S. Ammar-Merah, R. Brayner, F. Chau, M. Giraud, F. Mammeri, J. Peron, J. Y. Piquemal, L. Sicard, G. Viau, *Chem. Soc. Rev.* **2018**, *47*, 5187–5233.
- [36] R. Sheikhi, J. Cho, *J. Mater. Sci. Mater. Electron.* **2018**, *29*, 19034–19042.
- [37] R. J. Borg, G. J. Dienes, *An Introduction to Solid State Diffusion*, Academic Press, London, **1988**.

- [38] K. J. Carroll, J. U. Reveles, M. D. Shultz, S. N. Khanna, E. E. Carpenter, *J. Phys. Chem. C* **2011**, *115*, 2656–2664.
- [39] G. S. Okram, A. Soni, R. Prasad, *Adv. Sci. Lett.* **2011**, *4*, 132–135.
- [40] R. Eluri, B. Paul, *J. Nanopart. Res.* **2012**, *14*, 1–14.
- [41] J. Teichert, T. Doert, M. Ruck, *Dalton Trans.* **2018**, *47*, 14085–14093.
- [42] a) ICSD: Inorganic Crystal Structure Database, Vers. 4.3.0, FIZ-Karlsruhe, Eggenstein-Leopoldshafen, Germany, **2019**; b) M. Hellenbrandt, in: *Crystallogr. Rev.*, Taylor & Francis, **2004**, 17–22.
- [43] SAINT+: Area-Detector Integration Software, Version 8.34 A, Bruker AXS Inc., Madison, Wisconsin, USA, **2013**.
- [44] SADABS: Area-Detector Absorption Correction, Version 2014/4, Bruker AXS Inc., Madison, Wisconsin, USA, **2014**.
- [45] G. M. Sheldrick, *Acta Crystallogr. Sect. A* **2015**, *71*, 3–8.
- [46] G. M. Sheldrick, *Acta Crystallogr. Sect. C* **2015**, *71*, 3–8.
- [47] O. V. Dolomanov, L. J. Bourhis, R. J. Gildea, J. A. K. Howard, H. Puschmann, *J. Appl. Crystallogr.* **2009**, *42*, 339–341.
- [48] K. Brandenburg, *Diamond 4: Crystal and Molecular Structure Visualization*, Crystal Impact GbR, Bonn, Germany, **2017**.

---

Manuscript received: August 21, 2020  
Revised manuscript received: August 31, 2020